I&EC research
Industrial & Engineering Chemistry Research

Article

Controllable Synthesis of Core-Shell Bi@ Amorphous Bi2O3 Nanospheres with Tunable Optical and Photocatalytic Activity for NO Removal

Meijuan Chen, Yan Li, Zhenyu Wang, Yunxia Gao, Yu Huang, Jun-ji Cao, WingKei Ho, and Shun Cheng Lee

Ind. Eng. Chem. Res., **Just Accepted Manuscript** • DOI: 10.1021/acs.iecr.7b02497 • Publication Date (Web): 23 Aug 2017

ACS Publications

Industrial & Engineering Chemistry Research is published by the American Chemical Society. 1155 Sixteenth Street N.W., Washington, DC 20036

Controllable Synthesis of Core-Shell Bi@ Amorphous Bi_2O_3 Nanospheres with Tunable Optical and Photocatalytic Activity for NO Removal

Meijuan Chen[a,b], Yan Li[b,c], Zhenyu Wang[a,b], Yunxia Gao[b,c], Yu Huang[b,c,*,1] Junji Cao[b,c], Wingkei Ho[d], Shuncheng Lee[e]

[a]*School of Human Settlements and Civil Engineering, Xi'an Jiaotong University, Xi'an 710049, China*

[b]*Key Lab of Aerosol Chemistry & Physics，Institute of Earth Environment, Chinese Academy of Sciences, Xi'an 710061, China*

[c]*State Key Lab of Loess and Quaternary Geology (SKLLQG), Institute of Earth Environment, Chinese Academy of Sciences, Xi'an 710061, China*

[d]*Department of Science and Environmental Studies, The Education University of Hong Kong, Hong Kong, China*

[e]*Department of Civil and Environmental Engineering, The Hong Kong Polytechnic University, Hung Hom, Hong Kong*

*Corresponding author: Prof. Yu Huang
E-mail address: huangyu@ieecas.cn
Tel: 86-29-6233 6261

ABSTRACT:

The size, morphology and structure of Bi nanoparticle can significantly affect its photocatalytic performance. In this study, core-shell structured Bi@ amorphous Bi_2O_3 nanospheres were synthesized through one-step solvothermal method, and the reaction mechanisms on NO removal were proposed. It was found that Bi nanoparticles can generate charge carriers by surface plasma resonance (SPR) under visible light irradiation, while the surface amorphous Bi_2O_3 layer can facilitate the charge carriers' separation. The $Bi@Bi_2O_3$ sample with the synthesis time of 18 hours exhibited superior visible light photocatalytic activity for NO degradation, attributing to the suited size and suitable amorphous Bi_2O_3 layer. $\bullet O_2^-$, $^1O_2$ and •OH radicals were identified as the main reactive species involved in the photocatalysis processes. Moreover, the enhancement mechanisms of photocatalytic NO removal over $Bi@Bi_2O_3$ samples were discussed. This study demonstrated that the fabrication of core-shell structured $Bi@Bi_2O_3$ is a good strategy for effective air pollution control.

Keywords: $Bi@Bi_2O_3$; core-shell structure; SPR; NO removal

1. INTRODUCTION

The atmospheric concentration of nitrogen oxides (NO_x) is increasing due to the excessive consumption of fossil fuels, which can lead to the formation of acid rain and photochemical smog,[1] and can also cause diseases such as respiratory tract inflammation and carcinoma of the lungs.[2, 3] Selective catalytic reduction (SCR) and wet scrubbing process are efficient De-NO_x source control strategies at high concentration.[1] As an alternative to these NO_x control method, photocatalysis technique is attractive recently to remove NO_x at parts-per-billion (ppb) levels under ambient temperature and pressure in view of its merits of using abundant solar energy and of environmental friendly property.[4] However, the low quantum efficiency and the narrow light response range of traditional semiconductor photocatalyst TiO_2 have restrained its practical application.[5] Therefore, development of novel photocatalysts with high efficiency is crucial for effective air pollution control.

Recently, plasmonic photocatalysis has attracted more and more attentions because it is promising to overcome drawbacks like limited visible-light absorption ability and high charge carriers' recombination rate of photocatalysts via combining nanostructured plasmonic metals with semiconductor-based material.[6-10] When the oscillating frequencies of free electrons in metal nanoparticles (such as Au, Ag, Cu and Bi) and incoming photons are matched, it can give rise to the so-called surface plasmon resonance (SPR) which can trigger the subsequent redox reactions.[9, 11-13] Bismuth (Bi), endowed with unique electronic properties, has been found to display optical resonances whose spectral position and width are sensitive to sizes control, like Ag.[14, 15] Toudert et al theoretically illustrated that SPR band can be tuned in the whole near-ultraviolet, visible, and near-infrared range by changing the size and shape of bismuth nanoparticles.[16] Afterwards, bismuth nanospheres with a size range of 30~60 nm were prepared by Wang et al. to devote to the photodegradation of Rhodamine B (RhB) in visible light utilizing the SPR and they predicted the surface plasmon band shifted from UV to visible wavelength range with the size increase.[17] After that, Dong et al. disclosed the SPR mechanism and application of Bi nanoparticles with a size range of 100~200 nm in photocatalysis towards NO removal under UV light irradiation.[18] Although the

study of photocatalytic mechanism of bismuth is still controversial, it is undeniable that Bi could be an excellent photocatalytic material which deserves intensively investigation.

In general, the size, morphology and structures of Bi nanoparticles can significantly affect its photocatalytic performance.[11, 15] In recent years, core/shell morphology has attracted increasing attention because it can fulfill the diverse application requirements by tuning the surface functions and limiting the crystal nucleus size.[19-21] The shell coating enables the manipulation over the properties of the core material, leading to the increased functionality and stability.[22-24] For example, metal core@metal oxides shell nanocomposites are endowed with remarkable advantages as heterogeneous photocatalysts such as enhanced stability, prolonged lifetime of photo-generated carriers, increased interfacial charge transfer process.[20, 25-27] Considering the unique merits of core/shell structure and SPR effect of Bi, various methods have been adopted to construct Bi-based core/shell structure. It was reported a Bi@Bi_2O_3 nanostructure synthesized via a microwave-assisted solvothermal route exhibited an efficient photocatalytic activity towards rhodamine B and methyl orange (MO) under UV light.[28] Bi@Bi_2O_3@carboxylate-rich carbon core-shell nanosturctures were observed to have significantly enhanced photocatalytic activity in terms of MO degradation under visible light irradiation.[29] Cao et al explored the super-hydrophobic Bi@Bi_2O_3 surface with hierarchical porous dendritic structures through Bi surface self-passivation.[30] To the best of our knowledge, despite various studies on Bi@Bi_2O_3, the effect of the shell structure on the photocatalytic performance and the possibility of using it as a photocatalyst in NO degradation at ppb level have rarely been reported.

In this study, we prepared a core-shell structure photocatalyst with a bismuth core and an amorphous Bi_2O_3 shell to remove NO at ppb level under the visible light irradiation. Various characterization methods were used to evaluate its physicochemical properties. Both the growth mechanism and the reasons for excellent visible light performance depended on nanosize control of this material were explored deeply.

2. MATERIALS AND METHODS

2.1 Synthesis of core-shell Bi@Bi_2O_3 nanospheres

All solvents and reagents are of analytical grade and directly used without further purification. A series of $Bi@Bi_2O_3$ samples with core-shell structure were synthesized by a one-step solvothermal method, with $Bi(NO_3)_3 \cdot 5H_2O$ as a precursor and ethylene glycol as a complexing agent and reducing agent. In a typical procedure, 1 mmol of $Bi(NO_3)_3 \cdot 5H_2O$ and the same amount of $C_6H_{12}O_6$ were dissolved in 15 mL of ethylene glycol under vigorous stirring for 30 min. The mixture was then transferred to a Teflon-lined stainless steel autoclave (20 mL capacity) and kept in an electric oven at 160 °C for 18 h. The as-prepared sample denoted as $Bi@Bi_2O_3$-18 h was collected by centrifugation, washed several times with absolute ethyl alcohol and deionized water, and dried at 70 °C in an oven. In order to demonstrate the effect of the core-shell structure on the photocatalytic performance, $Bi@Bi_2O_3$ samples with the length of reaction time at 12, 24 and 48 h were synthesized under identical conditions, and the corresponding products were denoted as $Bi@Bi_2O_3$-12 h, $Bi@Bi_2O_3$-24 h and $Bi@Bi_2O_3$-48 h, respectively.

2.2 Characterization of $Bi@Bi_2O_3$ nanospheres

Various methods were used to characterize the physical and chemical properties of the different $Bi@Bi_2O_3$ structure samples. The crystallographic information of the samples was established by powder X-ray diffraction on a PANalytical XPert PRO X-ray diffractometer system. Morphological and structural investigations were carried out with scanning electron microscopy (SEM, ZEISS, SUPRA^{TM} 55) and transmission electron microscopy (TEM, JEOL, JEM-3010). Furthermore, bulk and surface compositional analyses for the prepared samples were performed with energy-dispersive X-ray spectroscopy (EDX/TEM, JEM-3010) and X-ray photoelectron spectroscopy (XPS, Thermo ESCALAB 250), respectively. The Fourier transform infrared spectroscopy (FTIR) spectra were recorded on a FTIR absorption spectrometer (Vertex 70, Bruker, Germany) with KBr as the diluent. Quantitative analysis of the carbon element gained from the elemental analyzer (vario III EL, Elementar, Germany). A Varian Cary 100 Scan UV-Visible system equipped with a labsphere diffuse reflectance accessory was used to obtain the reflectance spectra of the catalysts over a

range of 200–800 nm. After the sample was pretreated using nitrogen purging for 3 h at 343 K, the nitrogen adsorption and desorption isotherm at 77 K was measured by a Micrometritics Gemini 2390 system. To identify each type of reactive oxygen species, electron spin-resonance spectroscopy (ESR; ER200-SRC, Bruker, Germany) were prepared by mixing the as-prepared photocatalysts in solution with different trapping agents. Thus, 5,5-Dimethyl-1-Pyrroline-N-Oxide (DMPO) was employed to verify the formation of superoxide ($\bullet O_2^-$) and hydroxyl radicals ($\bullet$OH). 4-oxo-2,2,6,6-Tetramethyl-1-piperidinyloxy (4-oxo-TEMP) was used to detect singlet oxygen, and 2,2,6,6-Tetramethylpiperidine-1-oxyl (TEMPO) was used to characterize photo-generated electrons, respectively.

2.3 Photoelectrochemical measurements

The photoelectrochemical properties of Bi@Bi_2O_3 samples were evaluated using a Parstat 4000 electrochemical workstation (USA) in a conventional three-electrode cell, in which a platinum plate and Ag/AgCl electrode were used as counter electrode and reference electrode, respectively. In order to fabricate the working electrode, 50 mg Bi@Bi_2O_3 was dispersed into 5 mL 1 wt% Nafion ethanol solution to obtain homogeneous suspension through bath sonication. Then Bi@Bi_2O_3 films were modified on the fluorine doped tin oxide (FTO) conducting glass by dip coating and dried at room temperature. The current-time curves were measured at 0.2 V vs. Ag/AgCl in 0.1 mol L^{-1} Na_2SO_3 solution at ambient temperature under a 100 W LED lamp with wavelength of 420 nm. Electrochemical impedance spectroscopy (EIS) was measured at a frequency range of 0.1 Hz to 100 kHz with an 5 mV voltage amplitude under open-circuit voltage in 1mmol L^{-1} $K_3Fe(CN)_6$ and $K_4Fe(CN)_6$ solution.

2.4 Photocatalytic activity test

The photocatalytic activities of the as-prepared Bi@Bi_2O_3 samples were evaluated by NO removal through monitoring the decrease of NO in a continuous flow reactor at ambient temperature under visible light irradiation provided by a 300 W Xenon lamp (MICROSOLAR 300, Perfect Light, China). The rectangular reactor which was made

of stainless steel was covered with quartz glass and the volume of the reactor was 4.5 L (10×30×15 cm). Briefly, 0.1 g of the as-prepared photocatalyst was dispersed in 20 mL of deionized water by ultrasound. Then it was spread in a glass petri dish with diameter of 90 mm and dried at 70 ^{o}C to produce a homogeneous distributed material. After cooling to room temperature, the sample dish was placed in the dark chamber. The concentration of tested NO gas was about 400 ppb generated by diluting 50 ppm NO (N_2 balance) from a compressed gas cylinder with pure air generated from a zero-air generator (Model 1001, Sabio, USA), and the flow rate was controlled at 3 L/min. After the adsorption-desorption equilibrium among gases and photocatalysts was achieved, the lamp was turned on. The concentration of NO was continuously measured by a chemiluminescence NO_x (the sum of NO and NO_2) analyzer (Thermo Environmental Instruments Inc., model 42c). The removal rate of NO after irradiation was calculated according to the following equation:

$$\eta=(C_0-C_t)/C_0 \times 100\ \%$$

Where η is the NO removal rate, C_0 is the initial NO concentration, and C_t is the outlet stream NO concentration.

3. RESULTS AND DISCUSSION

3.1 Phase structures, morphologies and chemical compositions

XRD patterns of the as-prepared Bi@Bi_2O_3-12 h, Bi@Bi_2O_3-18 h, Bi@Bi_2O_3-24 h and Bi@Bi_2O_3-48 h samples were shown in Figure 1, which can be readily indexed as pure rhombohedral Bi (JCPDS no. 05-0519). The intensity of the diffraction peaks became stronger with the reaction time prolonged, demonstrating that the samples were crystallized better and no other impurity characteristic peaks like Bi_2O_3 were observed.

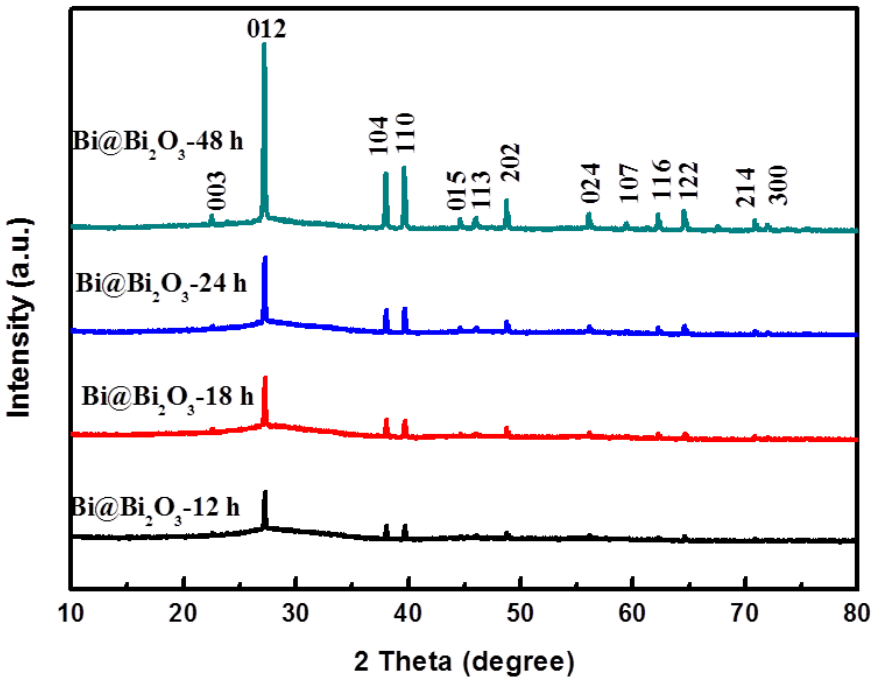

Figure 1. XRD Patterns of the as-prepared core-shell $Bi@Bi_2O_3$ nanoparticles ($Bi@Bi_2O_3$-12 h, $Bi@Bi_2O_3$-18 h, $Bi@Bi_2O_3$-24 h and $Bi@Bi_2O_3$-48 h).

SEM (Figure 2a-2d) and TEM (Figures 2e-2l) were used to characterize the morphologies of the as-prepared samples. The samples of $Bi@Bi_2O_3$-12 h, $Bi@Bi_2O_3$-18 h and $Bi@Bi_2O_3$-24 h were composed of uniform nanospheres with diameters of approximately 100 nm as shown in Figure 2a-2c. These monodispersed nanospheres can favor the transfer of charge carries, and this could improve the photocatalytic performance. However, the diameter of $Bi@Bi_2O_3$-48 h nanospheres was ranged from 100 nm to 1 μm, as illustrated in Figure 2d. This trend reveals that the size of $Bi@Bi_2O_3$ would not change when the synthesis time is within 24 h, but it could grow larger and larger if the reaction time prolonged.

TEM images confirmed that the as-prepared $Bi@Bi_2O_3$-12 h, $Bi@Bi_2O_3$-18 h and $Bi@Bi_2O_3$-24 h nanospheres had core-shell structures (Figure 2a-c). As shown in Figure S1, the shell thickness of $Bi@Bi_2O_3$-18 h is about 5 nm. With the synthesis time varying from 24 h to 48 h, the diameter of the Bi nanoparticles gradually increased. When the reaction time was set as 48h, the shell thickness is becoming much thinner

and the Bi nanoparticles grew up further with the diameter around 200 nm (See Figure 2h). As illustrated in Figure 2i-2l, HR-TEM results displayed that the clear lattice fringes with *d*-spacing of 0.328 nm corresponding to the (012) plane of Bi and no lattice striation was regarded as Bi_2O_3, as a further evidence for the presence of amorphous Bi_2O_3. The corresponding SAED patterns (inset in Figure 2i-2k) show multiple diffraction rings, indicating that the Bi mainly exist as polycrystal pattern until the hydrothermal reaction time to 24 h. When the time prolongs to 48 h, the single crystal Bi core was formed, confirmed by SAED diffraction spots in figure 2l. As shown in Figure S1, the EDS analysis for Bi@Bi_2O_3-18 h sample displayed that the sample was mainly consisted of Bi, O, and C, suggesting that the amorphous shell is Bi_2O_3 with few organic residuals.

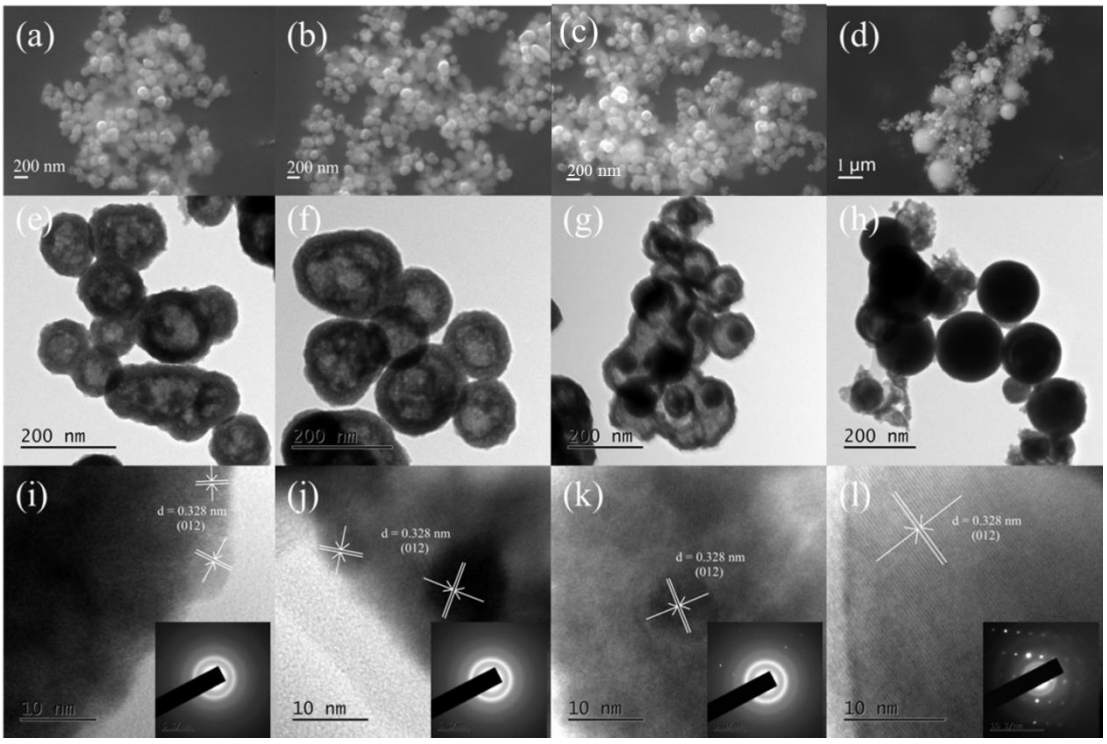

Figure 2. SEM images (a-d); low-magnification TEM images (e-h); HR-TEM images taken from the edge of the nanospheres (i-l); and SAED patterns of different core-shell structures (inset in i-l), respectively. the three images in the first to forth line is ascribed to Bi@Bi_2O_3-12 h、Bi@Bi_2O_3-18 h、Bi@Bi_2O_3-24 h and Bi@Bi_2O_3-48 h respectively.

The surface properties of different Bi@Bi_2O_3 samples were further investigated by FT-IR (Figure 3). The band at 513 cm^{-1} is attributed to the vibration of Bi-O bonds

in Bi_2O_3,[31, 32] which confirmed the existence of Bi_2O_3 in the as-prepared products. The peaks at 1611 and 1400 cm^{-1} are the characteristic asymmetric and symmetric stretching vibrations of COO^- groups, respectively. While the peaks at 1065 and 1120 cm^{-1} can be assigned to symmetric and asymmetric stretching vibration of C-O-C groups.[33, 34] These results indicated that carboxylate groups were coordinated strongly to the bismuth cations on the surface, the presence of which can contribute to a significant increase in the absorption intensity of hydroxyl groups. This is consistent with the result that the peak intensity at 3425 cm^{-1}, the hydroxyl stretching vibration of surface-adsorbed water and hydroxyl groups,[30] declined when the peak intensity of carboxylate groups at 1611 and 1400 cm^{-1} decreased. Furthermore, with the synthesis time prolonged from 12 h to 48 h, the characteristic peaks of Bi-O bonds are depressed gradually, suggesting the thickness of Bi_2O_3 gradually thinned, while the peaks of C-O-C groups at 1065 declined, suggesting the reduction of surface organic matter.

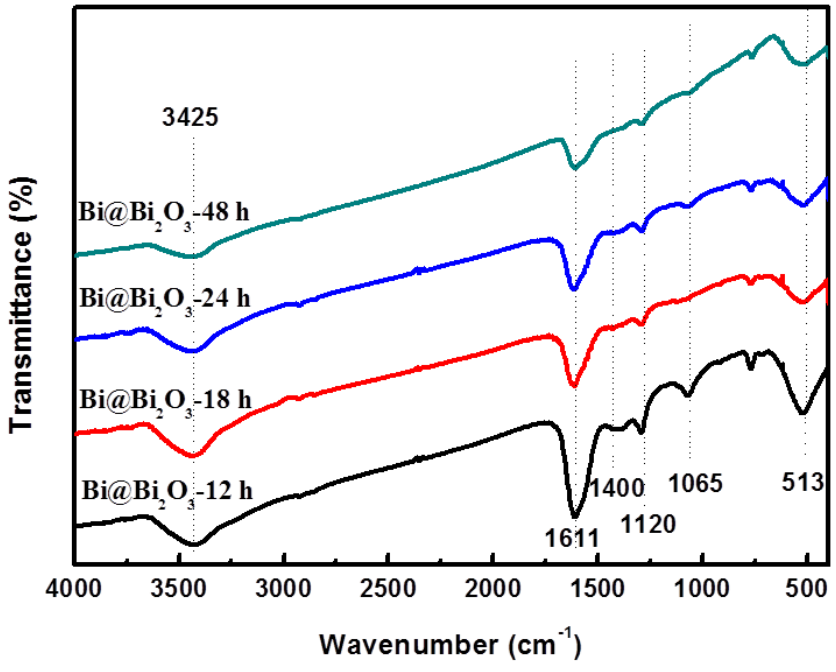

Figure 3. FT-IR spectra of the as-prepared $Bi@Bi_2O_3$ nanospheres

X-ray photoelectron spectroscopy (XPS) was used to identify the surface chemical states of $Bi@Bi_2O_3$ samples. The high-resolution XPS spectra and the percentage of elements (Bi 4*f*, C 1*s* and O 1*s*) in the as-prepared $Bi@Bi_2O_3$ samples before and after

being etched are shown in Figure S2a–S2d and Table S1. Typically, as shown in Figure 4, the Bi 4*f* spectra of Bi@Bi_2O_3-18 h sample before being etched were characterized by a Bi $4f_{5/2}$ peak at approximately 164.5 eV and a Bi $4f_{7/2}$ peak at 159.2 eV, which both belong to Bi-O in Bi_2O_3. After being etched, peaks at 162.3 eV and 157.0 eV were characteristic of the Bi-Bi bonds of elemental Bi.[35, 36] From sample Bi@Bi_2O_3-12 h to sample Bi@Bi_2O_3-48 h, the molar ratio of Bi-Bi/Bi-O was gradually increased (see Figure S2d), suggesting the core-shell structures were changed along with the synthesis time prolonged. C 1s spectra in Fig. S2b can be fitted into three peaks at 288.2, 286.0 and 284.7 eV, which correspond to the O-C=O, C-O, and C-C groups, respectively.[29 32] In addition, the XPS spectra in the O 1*s* region (Fig. S2c) also had three peaks. They stood for O-H at 532.9 eV, O-C at 531.2 eV and Bi-O at 529.7 eV, respectively, [37, 38] indicating the presence of surface organic matter and the amorphous Bi_2O_3. Furthermore, from Tab S1, the carbon contents obtained from elemental analyzer decrease with the reaction time increase from 12 h to 48 h. Thus, it can be inferred that the shell of the Bi nanospheres were composed of amorphous Bi_2O_3 and surface organic matter, the content both of which decreased with reaction time prolonged. These results are consistent with those of TEM and FT-IR.

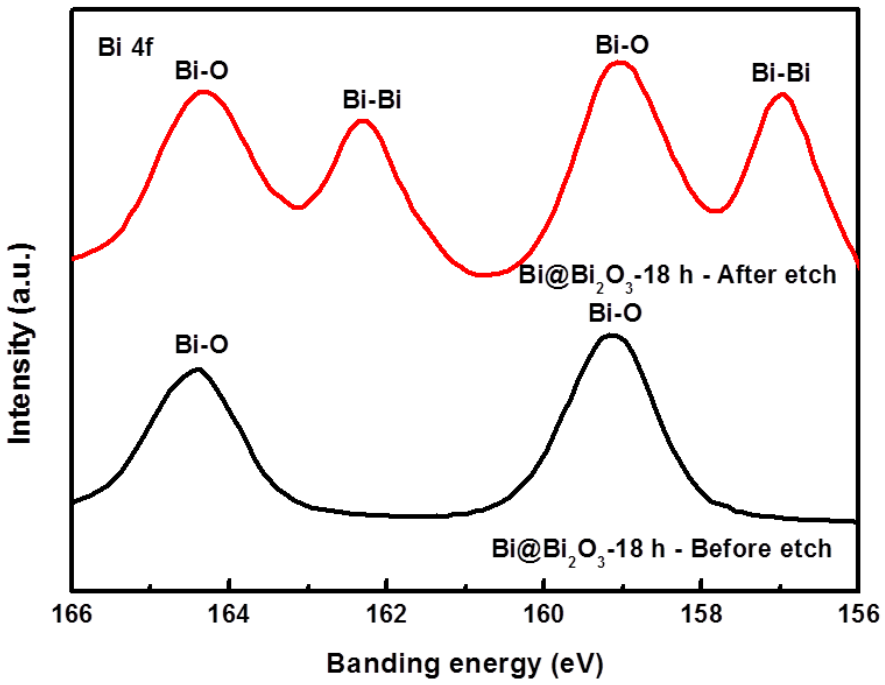

Figure 4. High-resolution XPS spectra of Bi 4f in Bi@Bi_2O_3-18 h before and after being etched for comparison

The nitrogen adsorption-desorption isotherm and pore size distribution curves (inset) of sample Bi@Bi_2O_3-18 h is shown in Figure S4. The physioadsorption isotherms of Bi@Bi_2O_3-18 h could be classified as type IV according to the IUPAC classification.[39] The pore size distribution was calculated from desorption branch of nitrogen isotherms by Barret-Joyner-Halenda (BJH) method using the Halsey equation. With the synthesis time prolonged, the specific surface areas of sample Bi@Bi_2O_3-12 h, Bi@Bi_2O_3-18 h, Bi@Bi_2O_3-24 h, and Bi@Bi_2O_3-48 h are 13.5, 14.6, 16.7, and 13.2 m^2/g, respectively. For samples Bi@Bi_2O_3-12 h, Bi@Bi_2O_3-18 h, Bi@Bi_2O_3-24 h, and Bi@Bi_2O_3-48 h the average pore diameter is around 45 nm, while it was reduced to 21.52 nm with the synthesis time prolonged to 48 h, which are negative for gas phase diffusion and exchange due to the narrow pore structure.

3.2 **Formation mechanism of core-shell Bi@Bi_2O_3 nanospheres**

On the basis of the above characterizations, the formation mechanism of core-shell Bi@Bi_2O_3 nanospheres with different synthesis time is proposed (Scheme 1). Firstly, $Bi(NO_3)_3 \cdot 5H_2O$ was dissolved in ethylene glycol (EG) to form coordination complexes between Bi^{3+} ions and EG.[36] Then glucose was added into the above solution. During the solvothermal synthesis process, glucose and ethylene glycol served as reducing agents, transforming Bi^{3+} to Bi^0 in the presence of a number of hydroxyl groups. The small Bi nanoparticles were not stable, and can react with hydroxyl groups to form amorphous Bi_2O_3 shell. Simultaneously, the condensation reaction of glucose and ethylene glycol resulted in the formation of the organic layer at high temperature. As this redox reaction and organic polycondensation reaction happened at the same time, the core-shell structure like Bi@Bi_2O_3-12 h and Bi@Bi_2O_3-18 h was formed with the components of bismuth element and bismuth oxide, as evidenced by the TEM and XPS analytical results. Along with the increase of reaction time, growing number of bismuth nanoparticles aggregated to form large bismuth particles via Ostwald ripening proces,[20] like Bi@Bi_2O_3-24 h. With synthesis time further prolonged, bismuth core grew larger

still with a thin amorphous Bi_2O_3 shell.

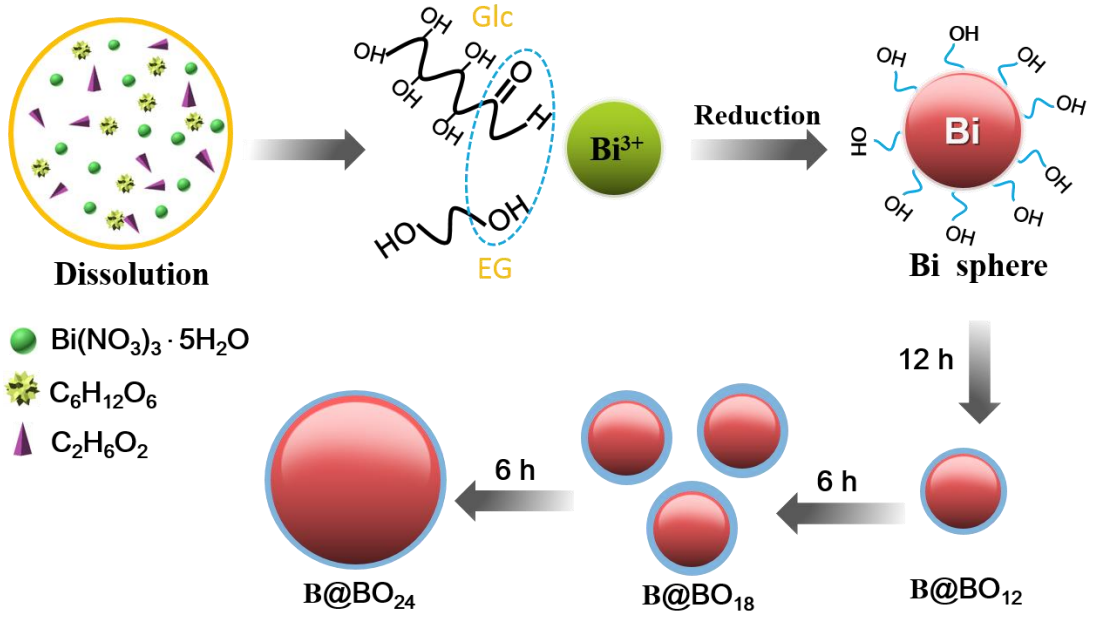

Scheme 1: Mechanism of core-shell $Bi@Bi_2O_3$ nanospheres formation by solvothermal method

3.3 **Photocatalytic performance on NO degradation**

The photocatalytic efficiency of the as-prepared $Bi@Bi_2O_3$ samples was evaluated by the degradation of NO under visible light irradiation. Figure 5 shows the variation of NO concentration (C/C_0) against irradiation time in the absence and presence of $Bi@Bi_2O_3$ samples. Here, C_0 is the initial concentration of NO, and C is the concentration of NO after photocatalytic degradation for time t. It was observed that the photolysis of NO without photocatalysts was negligible. In the presence of core-shell $Bi@Bi_2O_3$ samples, the NO concentration drastically decreased after the visible light was turned on, and it reached the steady state after about 10 min. The $Bi@Bi_2O_3$-18 h sample shows the highest NO removal rate up to 26.4%, while for $Bi@Bi_2O_3$-12 h, $Bi@Bi_2O_3$-24 h and $Bi@Bi_2O_3$-48 h, the NO removal rates were 20.9, 21.2 and 1.2%, respectively. Moreover, the toxic intermediate product NO_2 in the outlet gas was simultaneously monitored in the experiment. The NO_2 production was efficiently inhibited over the as-prepared core-shell $Bi@Bi_2O_3$ samples, suggesting the complete conversion of NO to NO_3^-. The $Bi@Bi_2O_3$-18 hsample exhibits the highest NO removal ratio and produces the lowest amount of NO_2, suggesting the superior NO

photocatalytic removal performance than that of other samples. From the aforementioned structure analysis results, the Bi@Bi_2O_3-18 h was endowed the largest average pore diameter, and suitable shell constituent and thickness. With the reaction time prolong to 24 h and 48 h， the small Bi cores begin to agglomeration and lead to the increased diameter of new Bi cores, which enhance the limitation of electron migration and potentiality to induce the production of $\bullet O_2^-$ and •OH due to size effect of SPR. The more details of that are discussed deeply in the next part.

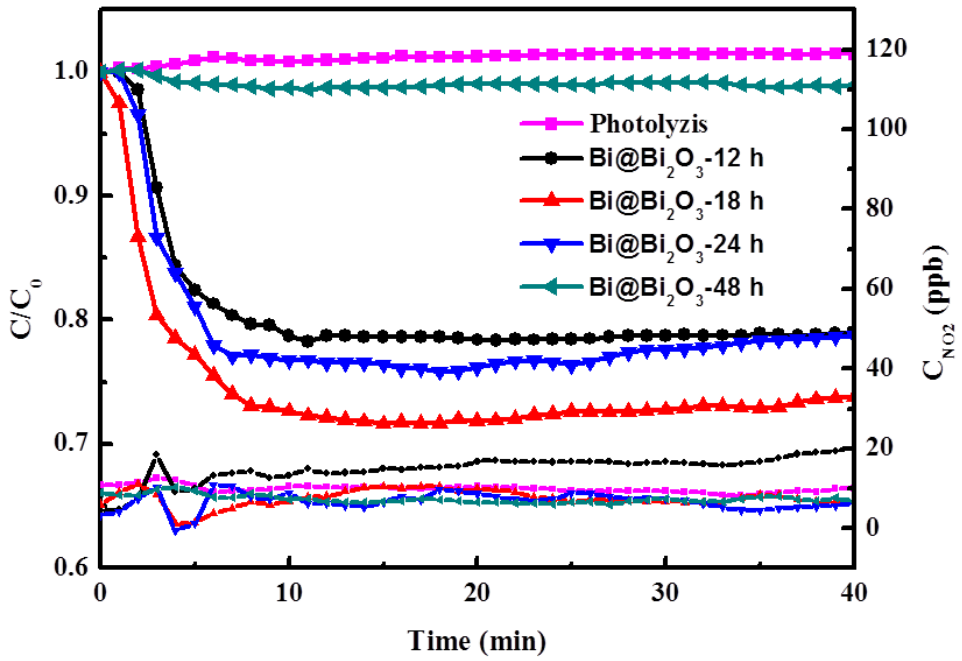

Figure 5. Photocatalytic activities of the as-prepared Bi@Bi_2O_3 samples for NO removal and NO_2 generation under visible light irradiation.

3.4 Mechanism on photocatalytic NO removal over core-shell Bi@Bi_2O_3 sample

3.4.1 Optical absorption and charge separation by photoelectrochemical studies

The typical UV-vis DRS spectral of the Bi@Bi_2O_3-18 h shown in Fig. 6 display the superior optical response at wavelengths ranging from 200 nm to 800 nm. Meanwhile, with increasing the reaction time, the visible light responses are enhanced especially for Bi@Bi_2O_3-48 h, which might be attributed to the increase content of Bi core. The nanosize of Bi core have two aspects influence on the SPR effects in light absorption. The one is that the SPR red shifted with the increase of the size. Toudert et al. has been

reported that metal Bi shows the SPR absorption equal to noble metal in visible and near ultra-violet range when the particle size of Bi is larger than 100 nm, agreeing with the UV-vis DRS spectral results.[40] J. McMahon et al. simulated the localized surface plasmon resonances of poor metals by using Mie theory and they found spherical bismuth with the size to 200 nm, the absorption bands boundary expanded to 700 nm.[41] The other is the different light scattering ability because of size distribution. Wang et al. calculated the bismuth nanospheres scattering efficiencies and the results showed that the contribution of scattering to the extinction band increases with the size.[17] So we believe that the visible light absorption of as-prepared products gradually increased with reaction time because of the increasing composition of Bi in $Bi@Bi_2O_3$ samples caused red shift SPR adsorption and light scattering extinction

.

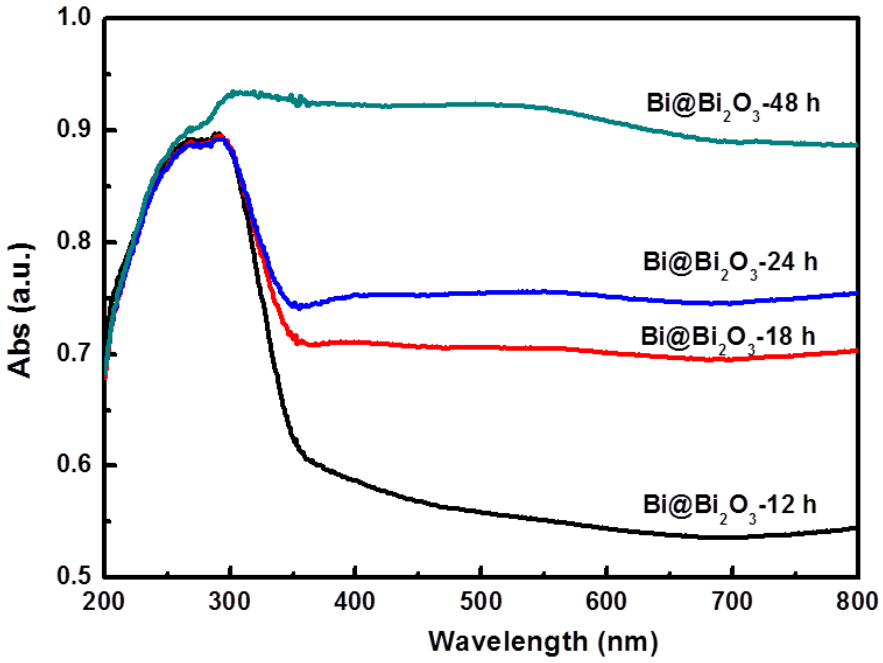

Figure 6. UV-vis absorption spectra of the products (with reaction time varying from 12 h to 48 h).

The transient photocurrent densities of the as-prepared $Bi@Bi_2O_3$ electrodes were tested under visible light irradiation. As shown in Figure 7a, the measured photocurrent densities of $Bi@Bi_2O_3$-12 h， $Bi@Bi_2O_3$-18 h and $Bi@Bi_2O_3$-24 h were roughly at the

same level (about 0.13 μA/cm^2). However, when the synthesis time was prolonged to 48 h, the photocurrent density of Bi@Bi_2O_3-48 h photoelectrode decreased significantly (about 0.08 μA/cm^2), suggesting that the presence of amorphous Bi_2O_3 shells played a critical role in the efficient separation of photogenerated electron-hole pairs.

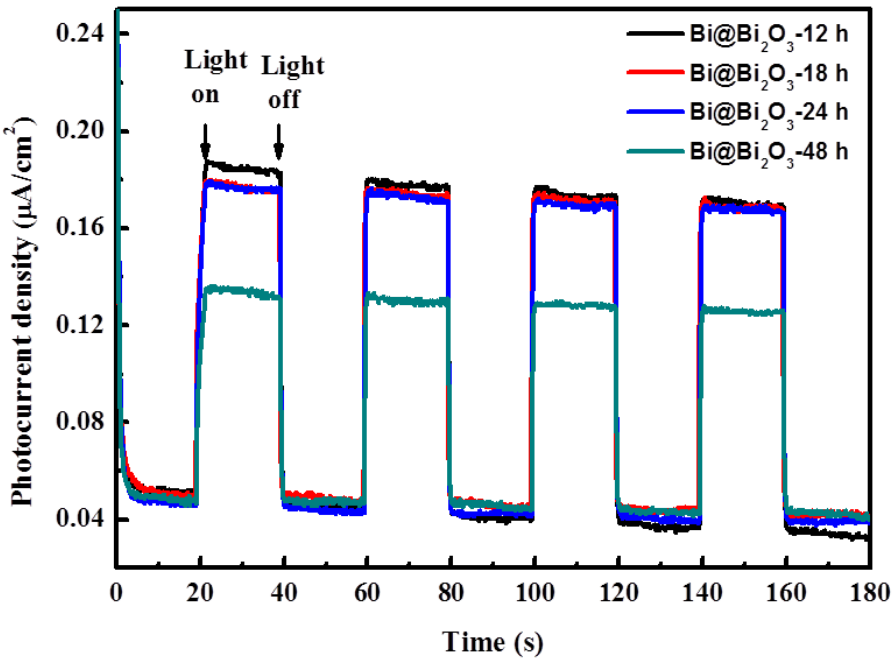

Figure 7. Photocurrent-time curves of the samples.

3.4.2 Active species identification by electron spin resonance (ESR) analysis

To further detect the involved active species during the photocatalytic process of NO removal, the ESR spectra of the sample Bi@Bi_2O_3-48 h were collected with different spin trapping agents. The ESR spectra were recorded with the irradiation time at 0 and 12 min for comparison (Figure 8). The signals of DMPO-•O_2^- and DMPO-•OH adducts were ignorable under dark conditions, while upon irradiation for 12 min in the presence of DMPO in methanol and aqueous dispersion, the significant characteristic peaks of DMPO-•O_2^- and DMPO-•OH adducts were clearly observed, suggesting the generation of superoxide radicals (•O_2^-) and hydroxy radicals (•OH) during the photocatalytic degradation processes[42]. Additionally, the singlet oxygen ($^1O_2$) was also identified due to the appropriate oxidizing power, which can be produced via the electron transfer

between superoxide and cation species.[29, 43] 4-oxo-TEMP was used to realize the identification of singlet oxygen, which could reacts with singlet oxygen to produce 4-oxo-2,2,6,6-tetramethylpiperidine-N-oxyl (TEMPONE, a three line spectrum with relative intensity ratio of 1:1:1). The significantly enhanced characteristic peaks of TEMPONE after irradiation confirmed the presence of singlet oxygen which could be the results that the hole traps one electron from $\bullet O_2^-$. Thus, we can infer that $\bullet O_2^-$, •OH and $^1O_2$ are the involved active species during the photocatalytic reactions.

Moreover, TEMPO, as the electrons capture agent, can be reduced to generate TEMPOH, and accompanied by flattening of the ESR signal.[43] Therefore, it can be employed to monitor the generation of photo-induced electrons and their reactivity by observing the change of ESR spectrum. There have three peaks for Bi@Bi_2O_3-18 h with a triplet spectrum of 1:1:1 in the dark, and these signal peaks are relatively stronger and stable. When TEMPO was irradiated, a visual decrease of TEMPO signal intensity was observed, suggesting that it was reduced by photo-generated electrons to an ESR-silent product (TEMPOH). That is to say, with the excitation of external light source, the generation of active electrons from core-shell Bi@Bi_2O_3-18 h sample is enhanced significantly, which is beneficial to photocatalytic reaction for NO removal.

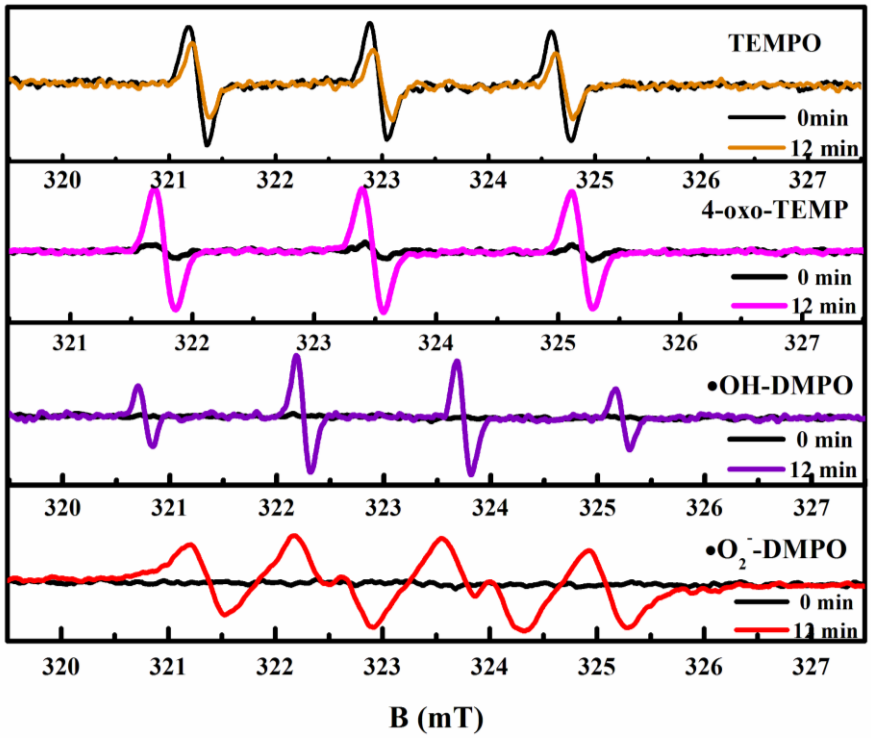

Figure 8. Spin-trapping ESR spectra under UV irradiation at wavelength of 280 nm for

0 and 12 min using different trapping agents in the presence of $Bi@Bi_2O_3$-18 h.

3.4.3 Mechanism for photocatalytic NO removal and activity enhancement of core-shell $Bi@Bi_2O_3$ samples for NO purification

Combined with various characterization results above, the photocatalytic correlation mechanisms of $Bi@Bi_2O_3$ was described as follow: firstly, similar to noble metal, semimetal bismuth as a direct plasmonic photocatalyst can show SPR effect under visible light irradiation due to the controllable nano-size and the SPR absorption can present red-shifted phenomenon because of the increase of the size. Thus, when the core part of Bi was excited, the SPR absorption position can determine the reduction and oxidation power of the photoinduced electrons and holes because of the different energy of resonance frequency wavelength.[44] In other words, electrons can be excited to lower bands SPR states and leave holes at higher one with the SPR absorption blue-shifted process. Dong et al. find that semimetal bismuth element show a poor photocatalytic activity towards NO removal when the potential of electrons or holes are not negative or positive enough to induce the production of $\bullet O_2^-$ and $\bullet OH$.[18] So, we deduced that $Bi@Bi_2O_3$-48 h with the largest size can produce resonance electron (as shown in Figure 7), but cannot induce activity free radicals, leading to a scarcely any NO removal effect. Secondly, amorphous Bi_2O_3 shell layer is closely connected with the surface of Bi core, which could be regarded as efficient electrons and holes acceptors to guide the directional transfer of photo-charges. Besides, the interface of Bi and Bi_2O_3 layer is presented as Bi_xO_y (x:y > 2:3) which might lead to the generation of positive charge centers which could trap electrons. When reaction time was set as 12 h, the as-obtained sample presents the thick amorphous Bi_2O_3 layer which is disadvantage to the photo-carriers toward the surface migration. On the contrary, with prolonging the reaction time, the significant reduced surface oxide layer lead to the photo-carriers separation being delayed for $Bi@Bi_2O_3$-48 h. Finally, as we known, the contact between gaseous pollutants and semiconductor, and even the effective photodegradation reaction occurs on the surface of semiconductor. Herein, the amorphous Bi_2O_3 shell provides the positive active site on account of the excellently absorption characteristics and could

protect Bi core from oxidation, which provided a safe environment for photocatalytic reaction. After timely separation of photo-generated electrons and holes on the surface reacted with oxygen and water molecules adsorbed on the surface of catalyst to form reactive species: $\bullet O_2^-$, $^1O_2$ and •OH, respectively. These three reactive oxygen species have the ability to oxide NO to form nitrate (NO_3^-) eventually as shown in scheme 2. That is why the surface oxide layer reduced caused a significant decrease NO removal ratio.

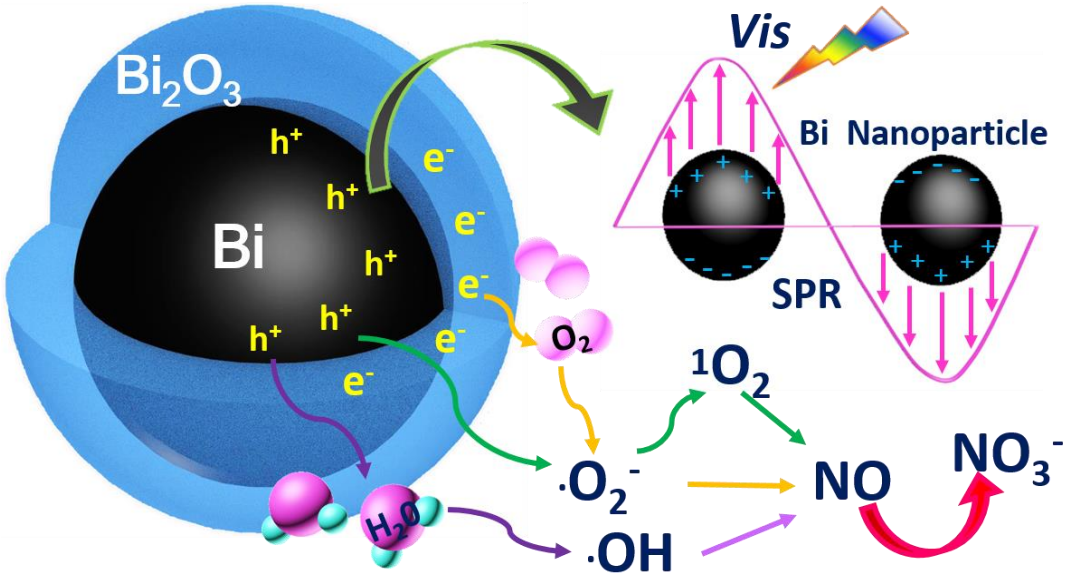

Scheme 2: Schematic diagram of the photocatalytic degradation mechanism of NO with $B@BO_{18}$ under simulated solar light irradiation.

4. CONCLUSION

In general, core-shell Bi@ amorphous Bi_2O_3 nanospheres were successfully synthesized by simple solvothermal method. The Bi core inside can be excited and show SPR effect under visible light irradiation due to the controllable nano-size and the SPR absorption can present red-shifted phenomenon because of the increase of the size. Thus, the $Bi@Bi_2O_3$-48 h sample with the largest size can show the strongest visible light harvest ability, but cannot induce reactive oxygen species, leading to a scarcely any NO removal effect. The $Bi@Bi_2O_3$-18 h sample exhibits superior visible light photocatalytic activity for the degradation of NO, attributing to the suited size and

suitable amorphous Bi_2O_3 layer which could prevent Bi from oxidation and help the efficiency separation of electrons-holes generated by surface plasma effect of Bi. The reaction and enhancement mechanisms of photocatalytic NO removal by the Bi@Bi_2O_3-18 h are discussed in detail.

ASSOCIATED CONTENT

Supporting Information

EDX of the Bi@Bi_2O_3-18 h nanospheres; High-resolution XPS spectra of Bi@Bi_2O_3-12 h, Bi@Bi_2O_3-18 h, Bi@Bi_2O_3-24 h and Bi@Bi_2O_3-48 h; Percentage of elements content in the as-prepared Bi@Bi_2O_3 before and after being etched for comparison; TGA profiles of Bi@Bi_2O_3-18 h powders; N_2 adsorption and desorption isotherms and pore-size distribution for Bi@Bi_2O_3-18 h; Summary of surface area, total pore volume and pore diameter of Bi@Bi_2O_3 for comparison. The Supporting Information is available free of charge on the publication website.

AUTHOR INFORMATION

Corresponding Authors

*E-mail: huangyu@ieecas.cn (Prof. Yu Huang).

Tel.: +86-29-62336261; Fax: +86-29-62336261

Notes

The authors declare no competing financial interest.

ACKNOWLEDGEMENTS

This research was financially supported by the National Natural Science Foundation of China (41503102), the China Postdoctoral Science Foundation (2015M572568), Shaanxi Postdoctoral Science Foundation (2016BSHEDZZ35) and the National Key

Research and Development Program of China (2016YFA0203000). Yu Huang is also supported by the "Hundred Talent Program" of the Chinese Academy of Sciences.

REFERENCES

(1) Lasek, J.; Yu, Y.-H.; Wu, J. C., Removal of NO x by photocatalytic processes. *J. Photoch. Photobio. C* **2013,** *14*, 29-52.

(2) Ibusuki, T.; Takeuchi, K., Removal of low concentration nitrogen oxides through photoassisted heterogeneous catalysis. *J. of Mol. Catal.* **1994,** *88*, 93-102.

(3) Negishi, N.; Takeuchi, K.; Ibusuki, T., Surface structure of the TiO2 thin film photocatalyst. *J. Mater. Sci.* **1998,** *33*, 5789-5794.

(4) Maggos, T.; Bartzis, J.; Leva, P.; Kotzias, D., Application of photocatalytic technology for NOx removal. *Appl. Phys. A* **2007,** *89*, 81-84.

(5) Dalton, J. S.; Janes, P. A.; Jones, N.; Nicholson, J. A.; Hallam, K. R.; Allen, G. C., Photocatalytic oxidation of NOx gases using TiO_2: a surface spectroscopic approach. *Environ. Pollut.* **2002,** *120*, 415-422.

(6) Wang, C.; Astruc, D., Nanogold plasmonic photocatalysis for organic synthesis and clean energy conversion. *Chem. Soc. Rev.* **2014,** *43*, 7188-7216.

(7) Rycenga, M.; Cobley, C. M.; Zeng, J.; Li, W.; Moran, C. H.; Zhang, Q.; Qin, D.; Xia, Y., Controlling the synthesis and assembly of silver nanostructures for plasmonic applications. *Chem. Rev.* **2011,** *111*, 3669-3712.

(8) Guo, X.; Hao, C.; Jin, G.; Zhu, H. Y.; Guo, X. Y., Copper nanoparticles on graphene support: an efficient photocatalyst for coupling of nitroaromatics in visible light. *Angew.*

Chem. Int. Edit. **2014,** *53*, 1973-1977.

(9) Zhang, Q.; Huang, Y.; Xu, L.; Cao, J.-j.; Ho, W.; Lee, S. C., Visible-Light-Active Plasmonic Ag–$SrTiO_3$ Nanocomposites for the Degradation of NO in Air with High Selectivity. *ACS Appl. Mater. Interfaces* **2016,** *8*, 4165-4174.

(10) Gao, Y.; Huang, Y.; Li, Y.; Zhang, Q.; Cao, J.-j.; Ho, W.; Lee, S. C., Plasmonic Bi/$ZnWO_4$ Microspheres with Improved Photocatalytic Activity on NO Removal under Visible Light. *ACS Sustain. Chem. Eng.* **2016,** *4*, 6912-6920.

(11) Gutiérrez, M.; Henglein, A., Nanometer-sized Bi particles in aqueous solution: absorption spectrum and some chemical properties. *J. Phys. Chem.* **1996,** *100*, 7656-7661.

(12) Li, X.; Sun, Y.; Xiong, T.; Jiang, G.; Zhang, Y.; Wu, Z.; Dong, F., Activation of amorphous bismuth oxide via plasmonic Bi metal for efficient visible-light photocatalysis. *J. Catal.* **2017,** *352*, 102-112.

(13) Wang, Z.; Yan, S.; Sun, Y.; Xiong, T.; Dong, F.; Zhang, W., Bi metal sphere/graphene oxide nanohybrids with enhanced direct plasmonic photocatalysis. *Appl. Catal. B: Environ.* **2017,** *214*, 148-157.

(14) Zhang, Q.; Li, W.; Moran, C.; Zeng, J.; Chen, J.; Wen, L.-P.; Xia, Y., Seed-mediated synthesis of Ag nanocubes with controllable edge lengths in the range of 30−200 nm and comparison of their optical properties. *J. Am. Chem. Soc.* **2010,** *132*, 11372-11378.

(15) Ni, Z.; Zhang, W.; Jiang, G.; Wang, X.; Lu, Z.; Sun, Y.; Li, X.; Zhang, Y.; Dong, F., Enhanced plasmonic photocatalysis by SiO_2@Bi microspheres with hot-electron

transportation channels via Bi–O–Si linkages. *Chinese J. Catal.* **2017,** *38*, 1174-1183.

(16) Toudert, J.; Serna, R.; Jimenez de Castro, M., Exploring the optical potential of nano-bismuth: tunable surface plasmon resonances in the near ultraviolet-to-near infrared range. *J.Phys. Chem.C* **2012,** *116*, 20530-20539.

(17) Wang, Z.; Jiang, C.; Huang, R.; Peng, H.; Tang, X., Investigation of optical and photocatalytic properties of bismuth nanospheres prepared by a facile thermolysis method. *J. Phys. Chem.C* **2013,** *118*, 1155-1160.

(18) Dong, F.; Xiong, T.; Sun, Y.; Zhao, Z.; Zhou, Y.; Feng, X.; Wu, Z., A semimetal bismuth element as a direct plasmonic photocatalyst. *Chem. Commun.* **2014,** *50*, 10386-10389.

(19) Zhao, J.; Han, Q.; Zhu, J.; Wu, X.; Wang, X., Synthesis of Bi nanowire networks and their superior photocatalytic activity for Cr (VI) reduction. *Nanoscale* **2014,** *6*, 10062-10070.

(20) Dong, W.; Zhang, L.; Li, B.; Wang, L.; Wang, G.; Li, X.; Chen, B.; Li, C., Preparation of hollow multiple-Ag-nanoclustes-C-shell nanostructures and their catalytic properties. *Appl. Catal. B: Environ.* **2016,** *180*, 13-19.

(21) Zhang, N.; Liu, S.; Xu, Y., Recent progress on metal core@semiconductor shell nanocomposites as a promising type of photocatalyst. *Nanoscale* **2012,** *4*, 2227-2238.

(22) Ghosh Chaudhuri, R.; Paria, S., Core/shell nanoparticles: classes, properties, synthesis mechanisms, characterization, and applications. *Chem. Rev.* **2011,** *112*, 2373-2433.

(23) Dai, R.; Wang, Y.; Da, P.; Wu, H.; Xu, M.; Zheng, G., Indirect growth of

mesoporous Bi@C core–shell nanowires for enhanced lithium-ion storage. *Nanoscale* **2014,** *6*, 13236-13241.

(24) Zhang, N.; Xu, Y., Aggregation- and Leaching-Resistant, Reusable, and Multifunctional Pd@CeO_2 as a Robust Nanocatalyst Achieved by a Hollow Core–Shell Strategy. *Chem. Mater.* **2013,** *25*, 1979-1988.

(25) Liu, B.; Zeng, H. C., Symmetric and asymmetric Ostwald ripening in the fabrication of homogeneous core–shell semiconductors. *Small* **2005,** *1*, 566-571.

(26) Zhang, N.; Liu, S.; Xu, Y.-J., Recent progress on metal core@ semiconductor shell nanocomposites as a promising type of photocatalyst. *Nanoscale* **2012,** *4*, 2227-2238.

(27) Ma, B.; Guo, J.; Dai, W.-L.; Fan, K., Highly stable and efficient Ag/AgCl core–shell sphere: controllable synthesis, characterization, and photocatalytic application. *Appl. Catal. B: Environ.* **2013,** *130*, 257-263.

(28) Kou, T.; Jin, C.; Zhang, C.; Sun, J.; Zhang, Z., Nanoporous core–shell Cu@ Cu_2 O nanocomposites with superior photocatalytic properties towards the degradation of methyl orange. *RSC Adv.* **2012,** *2*, 12636-12643.

(29) Liu, X.; Cao, H.; Yin, J., Generation and photocatalytic activities of Bi@ Bi_2O_3 microspheres. *Nano Res* **2011,** *4*, 470-482.

(30) Qu, L.; Luo, Z.; Tang, C., One step synthesis of Bi@ Bi_2O_3@ carboxylate-rich carbon spheres with enhanced photocatalytic performance. *Mater. Res. Bull.* **2013,** *48*, 4601-4605.

(31) Cao, L.; Lu, X.; Pu, F.; Yin, X.; Xia, Y.; Huang, W.; Li, Z., Facile fabrication of superhydrophobic Bi/Bi_2O_3 surfaces with hierarchical micro-nanostructures by

electroless deposition or electrodeposition. *Appl. Surf. Sci.* **2014,** *288*, 558-563.

(32) Zhu, Y.; Xu, D.; Meng, M., Ultrasonic-assisted synthesis of amorphous Bi_2S_3 coupled $(BiO)_2CO_3$ catalyst with improved visible light-responsive photocatalytic activity. *J. Mater. Sci.* **2015,** *50*, 1594-1604.

(33) Wang, C.; Shao, C.; Wang, L.; Zhang, L.; Li, X.; Liu, Y., Electrospinning preparation, characterization and photocatalytic properties of Bi_2O_3 nanofibers. *J. Colloid Interf. Sci* **2009,** *333*, 242-248.

(34) Sun, H.; Cao, L.; Lu, L., Magnetite/reduced graphene oxide nanocomposites: one step solvothermal synthesis and use as a novel platform for removal of dye pollutants. *Nano Res* **2011,** *4*, 550-562.

(35) Pan, C.; Zhu, Y., New type of $BiPO_4$ oxy-acid salt photocatalyst with high photocatalytic activity on degradation of dye. *Environ. Sci. Technol.* **2010,** *44*, 5570-5574.

(36) Dharmadhikari, V. S.; Sainkar, S.; Badrinarayan, S.; Goswami, A., Characterisation of thin films of bismuth oxide by X-ray photoelectron spectroscopy. *J. Electron Spectrosc* **1982,** *25*, 181-189.

(37) Zhu, C.; Guo, S.; Fang, Y.; Dong, S., Reducing sugar: new functional molecules for the green synthesis of graphene nanosheets. *ACS Nano* **2010,** *4*, 2429-2437.

(38) Yu, J. C.; Zhang, L.; Zheng, Z.; Zhao, J., Synthesis and characterization of phosphated mesoporous titanium dioxide with high photocatalytic activity. *Chem. Mater.* **2003,** *15*, 2280-2286.

(39) Lin, H.; Ye, H.; Li, X.; Cao, J.; Chen, S., Facile anion-exchange synthesis of

BiOI/BiOBr composite with enhanced photoelectrochemical and photocatalytic properties. *Ceram. Int.* **2014,** *40*, 9743-9750.

(40) Sing, K.; Everett, D.; Haul, R.; Moscou, L.; Pierotti, R.; Rouquerol, J.; Siemieniewska, T., Reporting physisorption data for gas/solid systems with special reference to the determination of surface area and porosity. *Pure Appl. Chem.* **1985,** *57*, 603-619.

(41) McMahon, J. M.; Schatz, G. C.; Gray, S. K., Plasmonics in the ultraviolet with the poor metals Al, Ga, In, Sn, Tl, Pb, and Bi. *Phys. Chem. Chem. Phys.* **2013,** *15*, 5415-5423.

(42) Dong, F.; Li, Q.; Sun, Y.; Ho, W.-K., Noble metal-like behavior of plasmonic Bi particles as a cocatalyst deposited on $(BiO)_2CO_3$ microspheres for efficient visible light photocatalysis. *ACS Catal.* **2014,** *4*, 4341-4350.

(43) Cao, S.; Zhou, P.; Yu, J., Recent advances in visible light Bi-based photocatalysts. *Chinese J. Catal.***2014,** *35*, 989-1007.

(44) Ke, X.; Sarina, S.; Zhao, J.; Zhang, X.; Chang, J.; Zhu, H., Tuning the reduction power of supported gold nanoparticle photocatalysts for selective reductions by manipulating the wavelength of visible light irradiation. *Chem. Commun.* **2012,** *43*, 3509-11.

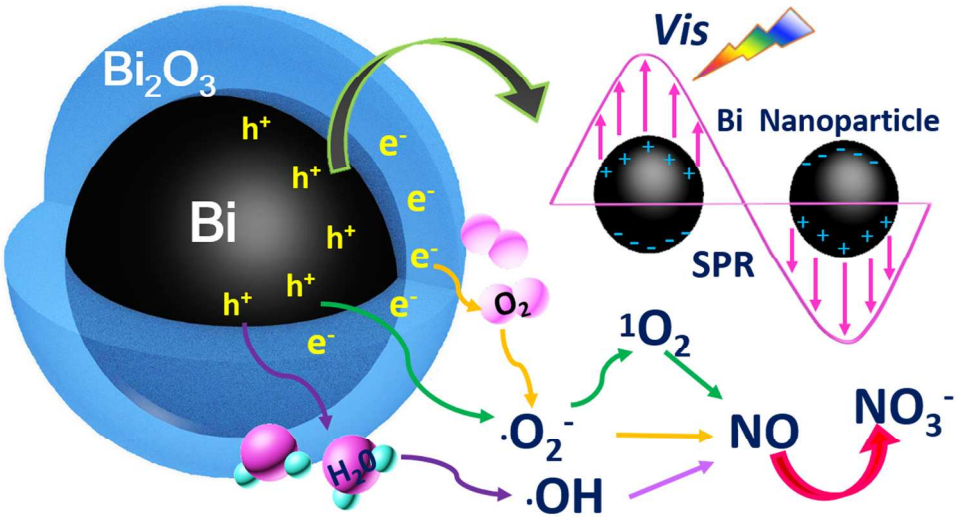

180x97mm (300 x 300 DPI)